Hydrol. Earth Syst. Sci. Discuss., 12, 13019–13067, 2015
www.hydrol-earth-syst-sci-discuss.net/12/13019/2015/
doi:10.5194/hessd-12-13019-2015

Hydrology and Earth System Sciences
Open Access
Discussions

Comparison of measured brightness temperatures from SMOS with modelled ones from ORCHIDEE and H-TESSEL over the Iberian Peninsula

A. Barella-Ortiz[1,5], **J. Polcher**[1,5], **P. de Rosnay**[2], **M. Piles**[3], **and E. Gelati**[4,5]

[1]Laboratoire de Météorologie Dynamique du CNRS, UMR8539, CNRS – IPSL, Paris, France
[2]European Centre for Medium-Range Weather Forecasts, Reading, UK
[3]Dept. de Teor. del Senyal i Comunicacions, Univ. Politec. de Catalunya, Barcelona, Spain
[4]CNRM-GAME (Météo-France, CNRS), Toulouse, France
[5]Centre National de la Recherche Scientifique (CNRS), France

Received: 3 September 2015 – Accepted: 2 November 2015 – Published: 15 December 2015

Correspondence to: A. Barella-Ortiz (anais.barella-ortiz@lmd.jussieu.fr)

Published by Copernicus Publications on behalf of the European Geosciences Union.

Abstract

L-Band radiometry is considered to be one of the most suitable techniques to estimate surface soil moisture by means of remote sensing. Brightness temperatures are key in this process, as they are the main input in the retrieval algorithm. The work exposed compares brightness temperatures measured by the Soil Moisture and Ocean Salinity (SMOS) mission to two different sets of modelled ones, over the Iberian Peninsula from 2010 to 2012. The latter were estimated using a radiative transfer model and state variables from two land surface models: (i) ORganising Carbon and Hydrology In Dynamic EcosystEms (ORCHIDEE) and (ii) Hydrology – Tiled ECMWF Scheme for Surface Exchanges over Land (H-TESSEL). The radiative transfer model used is the Community Microwave Emission Model (CMEM).

A good agreement in the temporal evolution of measured and modelled brightness temperatures is observed. However, their spatial structures are not consistent between them. An Empirical Orthogonal Function analysis of the brightness temperature's error identifies a dominant structure over the South-West of the Iberian Peninsula which evolves during the year and is maximum in Fall and Winter. Hypotheses concerning forcing induced biases and assumptions made in the radiative transfer model are analysed to explain this inconsistency, but no candidate is found to be responsible for it at the moment. Further hypotheses are proposed at the end of the paper.

1 Introduction

The United Nations (UN), the Food and Agriculture Organization (FAO), and the World Health Organization (WHO), have reported that water resources are not being managed in an optimum way nowadays. As a result, scarcity, hygiene and pollution issues related to improper water policies are detected. In addition, the world's population is expected to grow by 2 to 3 billion people over the next 40 years according to the UN's World Water Development Report (WWDR) from 2012. This will lead to a significant

HESSD
12, 13019–13067, 2015

increase in freshwater demand which will likely be affected by the effect of a changing climate.

To achieve a better management of water resources, it is necessary to improve our understanding of hydrological processes. In order to do this, the study of Soil Moisture (SM) is essential. It is defined as the water content in the soil and has a key role on the soil–atmosphere interface. SM determines whether evaporation over land surfaces is carried out at a potential rate (controlled by atmospheric conditions) or if it is limited by the available moisture (Milly, 1992). In addition, it influences several processes, like infiltration, which has an important effect on plant growth. However, SM is a complex variable to model in Land Surface Models (LSMs). For instance, the interaction between soil and water is not simple to represent. One way in which it is approached is through pedo-transfer functions (Marthews et al., 2014), which allow to estimate hydrodynamic characteristics of the soil from available soil properties' information regarding its texture and structure. It should be noted that the suitability of these functions is actually under debate, as their performance depends on several factors like the climate, geology, and the measurement techniques used. Furthermore, different hydrological schemes are found in models, leading to various ways of understanding and formulating soil moisture.

Remotely sensed soil moisture products have brought about new ways to perform data retrieval, adding new observations to data assimilation chains. The optimal combination of these products with modelled ones is expected to provide best estimates of the true soil moisture state. Remote sensing allows to estimate SM by means of retrieval algorithms, like inversion algorithms (Kerr et al., 2012) or neural networks (Kolassa et al., 2013). Their main input depends on the type of sensor used. This is, backscattering for an active sensor and Brightness Temperature (TB) for a passive sensor. TB corresponds to the radiance emitted by the Earth and is the magnitude measured by a radiometer. It is defined as the physical temperature times the emissivity of the surface.

HESSD
12, 13019–13067, 2015

L-Band radiometry is one of the best methods to estimate soil moisture, due to the relation between SM and the soil dielectric constant (ϵ) in this wavelength. The latter differs significantly between a dry soil and water (4 vs. 80, respectively) and this difference is key to obtain the soil water content. It should be noted that the retrieved SM corresponds to the water contained in the first centimetres of the soil. The penetration depth in averaged conditions is about 5 cm (Kerr et al., 2010). Other studies (Escorihuela et al., 2010; Entin et al., 2000) lower it to 1–2 cm, although it should be highlighted that information from thicker layers can also be retrieved due to the action of roots, for example. We will, therefore, talk about Surface Soil Moisture (SSM).

In the last decade, three space missions have been launched with L-band radiometers on-board: the Soil Moisture and Ocean Salinity (SMOS) mission (Kerr et al., 2010), the Aquarius/SAC-D mission (Le Vine et al., 2010), and the Soil Moisture Active and Passive (SMAP) mission (Entekhabi et al., 2010).

A large number of validation studies of remotely sensed SSM products have been carried out (Albergel et al., 2011; Sánchez et al., 2012; Bircher et al., 2013). These studies are usually performed using airborne and or ground-observed data over a well equipped site. Other studies, like the one described in González-Zamora et al. (2015), validate SMOS SSM products using in situ soil moisture measurement networks, which allow to extend the study period to annual and inter-annual scales. Several studies have been performed to validate brightness temperatures too (Rüdiger et al., 2011; Montzka et al., 2013). In Bircher et al. (2013) TBs are also validated with network and airborne data over a SMOS pixel in the Skjern river Catchment (Denmark). Coupled LSMs and Radiative Transfer Models (RTMs) can contribute to the analysis and validation of passive Microwave (MW) data. Models permit extending the validation to a longer period of time and perform an extensive analysis of observed and retrieved data, as showed in Schlenz el al. (2012). In this study, they compare TBs and vegetation optical depth from SMOS with modelled ones obtained from a coupled land surface and radiative transfer model, over a period of seven months in 2011 in the Vils test site (Germany). Comparing modelled with satellite-measured brightness temperatures can help to better

HESSD
12, 13019–13067, 2015

understand inconsistencies between retrieved and modelled data. It provides information regarding the origin of their differences, and whether they are due to the retrieval algorithm or to issues related to the modelling process.

In Polcher et al. (2015), the Level 2 (L2) SMOS product, corresponding to retrieved SSM, is compared to SSM modelled by the ORganising Carbon and Hydrology In Dynamic EcosystEms (ORCHIDEE) LSM (de Rosnay and Polcher, 1998; Krinner et al., 2005) over the Iberian Peninsula (IP) from 2010 to 2012. Even though a good agreement is observed in their temporal evolution, discrepancies are found between their spatial structures. The main objective of this paper is to extend the analysis of these discrepancies by comparing brightness temperatures measured by SMOS (Level 1C, L1C, product) with modelled ones obtained from the coupling of ORCHIDEE's state variables and a RTM. In addition, a second set of modelled TBs using state variables from the Hydrology – Tiled ECMWF Scheme for Surface Exchanges over Land (H-TESSEL), is included in the comparison. The RTM used is the Community Microwave Emission Model (CMEM) (de Rosnay et al., 2009), developed by the European Centre for Medium-Range Weather Forecasts (ECMWF). The comparison is performed over the same period and region as the study carried out by Polcher et al. (2015). The IP is an excellent test case for remote sensing of SSM, as the two climate regimes which characterize it (oceanic and Mediterranean) result in a strong contrast in soil water content. Furthermore, SSM is a critical variable regarding water resources especially in the Iberian Peninsula, which makes this study even more necessary.

The data from SMOS and the LSMs used in this paper will be presented in the next section, together with the methodology followed to model TBs. Next, the results will be presented. Firstly, modelled and measured TBs will be compared. Secondly, their error will be characterised spatially and temporally and certain hypotheses to explain the differences found in the TB comparison will be analysed. Finally, we will study the amplitude of the annual cycle of the TB signals. The paper will end with a discussion and conclusion section, proposing some further analyses to identify the cause of the inconsistency found between modelled and measured TBs.

HESSD
12, 13019–13067, 2015

2 Data and methods

2.1 SMOS data

The SMOS mission is the second Earth Explorer Opportunity mission from the European Spatial Agency (ESA). The SMOS satellite was launched on 2 November 2009. One of its main objectives is to provide surface soil moisture over land with a target accuracy of 0.04 $m^3 m^{-3}$.

As previously said, TBs are the main input of SMOS's soil moisture retrieval algorithm. L-band brightness temperatures are measured by the SMOS radiometer at different incidence angles (from 0 to 65°) and polarizations (H, V, HV). Modelled TBs are also computed using the state-of-the-art L-band Microwave Emission of the Biosphere (L-MEB) forward model (Wigneron et al., 2007) with some modifications. These data are then used to retrieve SSM using an inversion algorithm based on an iterative approach. Its objective is to minimize the sum of the squared weighted differences between measured and modelled TBs for all available incidence angles. Details about the retrieval algorithm are provided in Kerr et al. (2012).

The SMOS L1C v5.05 product over the 10° W–5° E to 45–35° N region was selected and SMOS TBs at the antenna reference plane were derived. These TBs have been first screened out for Radio-Frequency Interferences (RFIs) (strong, point source and tails), and also for Sun (glint area, aliases and tails), and Moon (aliases) contamination, using the corresponding flags. Ionospheric effects (geometric and Faraday rotations) are later corrected to obtain TB at the Top Of the Atmosphere (TOA). TB maps at a constant incidence angle of 42.5 ± 5° are obtained through chi squared linear fit of all values included in the interval 42.5 ± 5°, which is the methodology used to generate the SMOS L1C browse product (McMullan et al., 2008). Finally, these maps are resampled from the Icosahedral Snyder Equal Area (ISEA) 4H9 grid to a 0.25° regular latitude–longitude grid, which is easier to manipulate.

HESSD
12, 13019–13067, 2015

The L1C product containing horizontally and vertically polarized brightness temperatures, was provided by the SMOS Barcelona Expert Center. From now on, this product will be referred to as TB_{SM}.

2.2 Radiative transfer model and land surface models

The two sets of modelled TBs were estimated by means of the CMEM, which was provided with state variables from ORCHIDEE and H-TESSEL simulations. These sets will be referred to as TB_{OR} and TB_{HT}, respectively.

2.2.1 CMEM

The Community Microwave Emission Modelling (CMEM) Platform, (https://software.ecmwf.int/wiki/display/LDAS/CMEM) developed by the ECMWF, is the forward operator for low frequency passive MW brightness temperatures of the surface. Its physics is based on that from the L-MEB forward model and the Land Surface Microwave Emission Model (LSMEM) (Drusch et al., 2001). CMEM is characterized by its modular structure, which allows the user to choose among different physical configurations to compute TB's key parameters. For example, the soil dielectric constant or the vegetation optical depth. Polarized brightness temperatures provided at TOA result from the contribution of three dielectric layers: atmosphere, soil and vegetation. Snow, also considered, is characterized as a single additional homogeneous layer.

The configurations defined in CMEM for each set of modelled TBs are listed in Table 1. The physical configuration of the set using ORCHIDEE's state variables was selected to be as similar as possible to the set using H-TESSEL's output. However, they differ in the parametrization used to compute the smooth surface emissivity (ε_s). The reason being that Wilheit (1978) was chosen in TB_{OR}'s case, because it is more physically based, and with no a priori assumption on the sampling depth, than the Fresnel law (used for TB_{HT}). It considers the soil as a stratified medium and it allows taking advantage of ORCHIDEE's finer soil discretization. For instance, Parrens et al. (2014)

HESSD
12, 13019–13067, 2015

study the added value of using a multilayer soil model to simulate TBs and show that the Wilheit parametrization improves modelled TBs. The different parametrizations chosen to calculate ε_s lead to another variation between the CMEM configurations. If ε_s is computed using Wilheit (1978), the soil temperature profile is used to compute the Effective Temperature (T_{eff}). On the contrary, if the Fresnel law is used, the user can choose among different parametrizations to compute T_{eff}. For TB_{HT}, Wigneron et al. (2001) was selected.

Differences in the CMEM observing and soil configurations are also found. Each set considers a different incidence angle. Although TB_{HT} were modelled considering an angle of 40°, it was decided to set it to 42.5° to model TB_{OR}, because measured TBs were provided at this angle. As for the soil configuration, a different number of soil layers is considered for each TB set: 11 (TB_{OR}) and 3 (TB_{HT}). ORCHIDEE's soil discretization is finer. For instance, its first layer's depth is of the order of millimetres, while H-TESSEL's is of centimetres. Keeping each model's discretization allowed us to study whether this difference had an impact on modelled TBs.

The variables required by the CMEM to model TBs can be classified into dynamic and constant fields that consist of meteorological data, vegetation characteristics and soil conditions. They are summarized in Table 2.

2.2.2 Land surface models

Several differences can be identified between the ORCHIDEE and the H-TESSEL LSMs. We will focus on their hydrological schemes, and provide some information about the soil and land surface temperatures in each model. The reason being that SM and temperature state variables are key inputs in the CMEM.

The hydrological scheme used by ORCHIDEE is based on the model of the Centre for Water Resources Research (CWRR). It approaches hydrology through the resolution of a diffusive equation over a multilayer scheme. For this, the Fokker–Planck equation is solved over a soil 2 m deep with an 11 layer discretization. The H-TESSEL scheme also solves a diffusive equation over a multilayer scheme. However, it consid-

HESSD
12, 13019–13067, 2015

ers a 4 layer discretization, with the layer's depth following an approximate geometric relation (7 cm for the first one, 21, 72, and 189 cm for the other three). In addition, the soil can be covered by a single snow layer. We would like to recall the difference between the first soil layer's depth of both models.

In ORCHIDEE and H-TESSEL the bottom boundary condition assumes free drainage under the hypothesis that the water content gradient between the last modelled layer and the next one (not modelled) is zero. However, both models differ in the upper boundary condition. While in ORCHIDEE the bare soil evaporation is the maximum upward hydrological flux which is permitted by diffusion if it is lower than potential evaporation, in H-TESSEL the upper boundary condition is infiltration plus surface evaporation. It considers a maximum infiltration rate given by the maximum downward diffusion from the saturated surface. Once this rate is exceeded by the water flux at the surface, the excess of water is derived to surface runoff.

The CWRR scheme considers a sub-grid variability of soil moisture, which together with the fine soil discretization improves the representation of infiltration processes. In ORCHIDEE, the soil infiltration follows the Green–Ampt equation (Green and Ampt, 1911) to represent the evolution in time of the wetting front through the soil layers. It should be noted that partial re-infiltration occurs from surface runoff if the local slope of the grid-cell is $\leq 0.5\,\%$ (D'Orgeval et al., 2008). Each grid box has a unique soil texture and structure (Post and Zobler, 2000), but three different soil columns are considered, each one with a soil moisture reservoir and a root profile assigned. These are classified as: bare soil, low and high vegetation. They take into account the 13 plant functional types defined in ORCHIDEE. The water balance is solved for each soil type resulting in three different soil moisture profiles in each grid box. In H-TESSEL, six types of tiles are considered over land: bare soil, low and high vegetation, water intercepted by leaves, as well as shaded and exposed snow. Each one of these has its own energy and water balance. However, only one soil moisture reservoir is considered. Recent improvements have replaced a globally uniform soil type (loamy) by a spatially varying

HESSD
12, 13019–13067, 2015

one (coarse, medium, medium-fine, fine, very fine, organic). Surface runoff, based on variable infiltration capacity, was also a recent improvement (Balsamo et al., 2009).

In ORCHIDEE the soil temperature profile is calculated solving the heat diffusion equation. Contrary to the hydrological scheme, it considers a 7 layer discretization, where the layers' thicknesses follow a geometric series of ratio 2, and a total soil depth of 5.5 m. For this study, the first 2 m of ORCHIDEE's temperature profile were calculated following the same soil discretization as the one considered in the soil moisture calculation. In H-TESSEL, the same soil discretization as the one defined in its hydrological scheme is used to calculate the soil temperature. The soil heat budget follows a Fourier diffusion law, which has been modified to consider also thermal effects caused by changes in the soil water phases (Holmes et al., 2012). ORCHIDEE's energy balance takes into account the skin temperature as presented in Schulz et al. (2001) to derive the Land Surface Temperature (LST). The soil and vegetation are considered as a single medium assigned with a surface temperature (Santaren et al., 2007). As for H-TESSEL, a skin layer is defined representing (i) the layer of vegetation, (ii) the top layer of bare soil, or (iii) the top layer of the snow pack. To calculate the LST, the surface energy balance equation is linearised for each tile (Viterbo and Beljaars, 1995).

Both LSMs were forced with the ERA-Interim forcing (Dee et al., 2011), which is suitable for this study because it ranges from 1979 to 2012 and near current data was needed to perform the comparison with SMOS's data. We are aware that biases in this kind of forcings have an effect on the LSMs simulations (Ngo-Duc et al., 2005). ORCHIDEE's simulation was configured to output hourly data in order to compute hourly TB values, as TB_{SM}. However, TB_{HT} is output at 6 hourly time steps (at 0, 6, 12, and 18 h). Due to this difference, each set of modelled TBs was sampled in a different way using SMOS's TBs. The sampling processes will be explained in the next subsection.

2.3 Brightness temperature comparison

To compare modelled and measured brightness temperatures, TB_{OR} and TB_{HT} were sampled with TB_{SM} and remapped to the nearest neighbour of the SMOS grid. This

HESSD
12, 13019–13067, 2015

allowed us to keep the spatial structures of the coarse model resolution. Next, the three TB signals were filtered to avoid certain effects due to frozen soils or RFIs, among other causes.

2.3.1 Sampling

The objective of sampling the data is to use only modelled TBs corresponding to available measured values. TB_{OR} were sampled at an hourly scale. Since H-TESSEL's surface state variables consist of a value each 6 h, an hourly sampling resulted in data being neglected because TB_{HT}'s hours did not always correspond to those from SMOS's observations. Therefore, TB_{HT} were sampled considering a 3 h window of TB_{SM} in order to keep a larger number of modelled data for the comparison. To test the impact of the 3 hourly sampling we also performed it using the TB_{OR} set and compared it with the hourly sampled one. Differences between them were under 0.1 %, and thus it was considered to be negligible.

2.3.2 Filtering

Data was filtered to discard unreasonable TB values from the comparison study. Modelled TB_{HT} was provided already filtered, following the criteria of the ECMWF. Therefore, we decided to filter TB_{OR} using a criteria that followed the same objectives as those from the ECMWF. Common filters were also applied to measured and modelled data. All of them are summarized in Table 3.

The filters applied in TB_{HT} corresponding to the water content in snow cover (snow water equivalent) and the criterion on the ERA-Interim forcing's 2 m temperature aim to discard frozen soils, which might affect the SM retrieval (Dente et al., 2012). The same purpose was followed to filter TB_{OR}, using the 2 m temperature from the forcing (as in the previous case) as well as ORCHIDEE's average surface temperature. Concerning the common criteria, one of them is to exclude TBs higher than 300 K and the other one consists on applying a mask. The first one aims at avoiding effects of RFIs, which can

HESSD
12, 13019–13067, 2015

result in overestimated brightness temperatures (higher than 1000 K). The second one aims at removing points which might be influenced by coastal or topographic effects, as does H-TESSEL's orography (slope) criterion too. The mask was built using the L2 SMOS product. Any pixel with no surface soil moisture data retrieved, together with the 24 pixels surrounding it, was excluded from the comparison study.

3 Results

In this section, the temporal evolution and spatial structures of measured and modelled TBs will be compared. This study was performed after the comparison between SSM modelled by ORCHIDEE and retrieved by SMOS (Polcher et al., 2015), where an inconsistency was found between their spatial structures. The TB comparison allows to study whether these differences can be explained by the retrieval algorithm or the modelled SSM.

3.1 Comparison of modelled and measured brightness temperatures

The temporal correlation between modelled and measured TBs is computed to compare their temporal evolution, and the spatial correlation to analyse the relation between their spatial patterns. The mean values of both correlations, over the Iberian Peninsula from 2010 to 2012, are shown in Table 4, together with those for the SSM comparison (Polcher et al., 2015). We will refer to these results throughout this section.

Figure 1 shows the temporal correlation between observed and modelled daily TB for the horizontal and vertical polarizations. Values are statistically significant at 95 % level. Both polarizations show a good agreement between models and observations, with values higher than 0.7 over a large part of the IP. This result was expected due to the strong annual cycle described by the surface temperature and especially to the quick response of temperature to precipitation that drives TB's fast varying component. The high correlations indicate that this response, which corresponds to the synoptic

HESSD
12, 13019–13067, 2015

variability of the TB signal, is well captured by both models. Most of the areas with lower correlations correspond to mountain chains. Relief effects on MW radiometry over land (Mätzler and Standley, 2000) are a difficult remote sensing problem and thus, discrepancies are expected. In fact, the lowest correlations (0.3 to 0.6) appear over some areas of the Pyrenees. Other examples are the Iberian System and the Cantabrian Mountains, located over the North-Eastern and the Northern regions of the peninsula, respectively.

There are no large differences in Fig. 1 between the TB_{OR} (upper row) and the TB_{HT} (lower row) regarding their temporal correlation with TB_{SM}. Since the same forcing was used for both simulations, the two LSMs share the same synoptic variability from the ERA-Interim reanalysis. However, Fig. 1 shows that the synoptic variability of H-TESSEL leads to slightly higher correlation values than ORCHIDEE's, specially over the northern part of the IP.

The temporal correlations obtained between TB_{OR} and TB_{SM} are very similar to those found when retrieved SSM from SMOS was compared to modelled one from ORCHIDEE. The mean correlations are 0.75 (horizontal polarization) and 0.76 (vertical polarization) for the TBs and 0.81 for the SSM. In addition, lower SSM correlation values are also observed over regions correspondent to mountain chains. Therefore, a good agreement in the temporal evolution of both variables is found between modelled and observed/retrieved data. It should be noted that in the study performed for the SSM data, the correlation appears to be driven by the SSM's fast component, which is related to its rapid response to rainfall events. Consequently, the correlation analysis does not provide reliable information regarding the annual cycle of the SSM.

The spatial correlation between measured and modelled TBs provides a first analysis of the consistency of their spatial structures. To have the highest coverage as possible, an averaging window of 5 days is considered. For clarity, the 5 daily correlations are grouped per season and the distribution of values obtained are represented in a boxplot form in Fig. 2. The values shown are statistically significant at 95 % level. First of all, it can be seen that the correlations are generally poor throughout the year.

HESSD
12, 13019–13067, 2015

Although maximum values are around 0.6, the mean annual correlations are between 0.20 and 0.30 (Table 4). In addition, a seasonality can be identified in the correlation of TB_{SM} with both sets of modelled TBs. The lowest correlations occur during the Winter season, where even negative values are obtained. These improve during Spring and Summer, and weaken again in Fall. Moreover, Winter and Fall generally show larger ranges of variability and thus, a wider dispersion of the data than Spring and Summer.

The boxplot provides further information. For instance, it shows that the vertical polarization has systematically a higher mean correlation than the horizontal one, except for the Winter season. As for the comparison between the two sets of modelled TBs, there is no significant difference between them. The mean correlation between measured and modelled TBs is higher in Winter if TB_{OR} is used, instead of TB_{HT}. However, the opposite behaviour is observed for the rest of the seasons.

Summarizing, the spatial structures from modelled TBs are not consistent with those observed by SMOS, especially in Fall and Winter. A similar result was obtained for the comparison between measured and modelled SSM. This can be seen in Table 4, where the mean spatial correlation between SMOS's and ORCHIDEE's SSM is 0.28. Nevertheless, the temporal evolution of the SSM spatial correlation does not show the same seasonal variation as the one identified for TBs. For SSM, similar correlations are observed throughout the years, with no significant differences between seasons. This suggests that the origin of the weak spatial correlation shown by both TBs and SSM may be due to different processes.

3.2 Temporal and spatial characterization of the error

To better understand the inconsistency between spatial structures found in the previous subsection, we choose to study the spatio-temporal variability of the error between modelled and measured TBs. Our aim is to analyse if this difference can be (fully or partly) explained by spatially coherent patterns connected to a physical process. In order to do that, an Empirical Orthogonal Function (EOF) analysis (Björnsson and Venegas, 1997) of the TB error is performed. This method allows to extract the dominant

HESSD
12, 13019–13067, 2015

spatial and temporal modes of variability of a field. It relates the spatial patterns of each variation mode together with their temporal evolution and with the explained variance.

An example of this methodology applied to error analysis is given in Kanamitsu et al. (2010), where they study the impact of a regional model error on the inter-annual variability of a set of analysis fields. Identifying the main modes of variability of the error allows to propose hypotheses to explain its physical cause, as well as to discard them if the modes' patterns and temporal evolution do not resemble to those expected by the hypothesis suggested. We will also be able to study similarities between the two LSMs, by comparing the results obtained for the EOF analysis of each TB error, as well as the similarities between the TB error and other variables' errors.

3.2.1 TB error

Figure 3 shows the spatial patterns of the first two EOF variation modes correspondent to the TB error of ORCHIDEE ($TB_{OR} - TB_{SM}$), for the horizontal (upper row) and the vertical (lower row) polarizations. The variance explained by each mode is also provided as a percentage in brackets. The pattern of the first variation mode explains 36 % (horizontal polarization) and 31 % (vertical polarization) of the total variance and is very similar in both polarizations. In fact, a correlation of 0.99 is obtained between them. This value, together with further correlations regarding the spatial patterns of the EOF analysis, is listed in Table 5. The spatial patterns show a structure characterised by high values over the South-West and a smaller area further North of the IP, which weaken as they extend through the rest of the peninsula. The second variation mode of the TB error of ORCHIDEE exhibits a pattern with a structure that is also maximum over the South-West of the IP in both polarizations. However, the total variance explained is reduced to 6 and 7 % (horizontal and vertical polarization, respectively).

The spatial patterns of the first two EOF modes obtained for the TB error of H-TESSEL ($TB_{HT} - TB_{SM}$) are shown in Fig. 4. Compared to the error of ORCHIDEE, the percentage of variance explained by the first variation mode is reduced to 30 and 18 % for the horizontal and vertical polarization, respectively. As occurred in the previ-

HESSD
12, 13019–13067, 2015

ous case, the spatial structures of the first mode's horizontal and vertical polarizations coincide. A correlation of 0.86 is obtained between them. Furthermore, these patterns show similar spatial structures to those from the patterns found for the first variation mode of the TB error of ORCHIDEE (Fig. 3a and c). This is confirmed by the correlations obtained between the patterns of both errors: 0.92 and 0.73 for the horizontal and vertical polarization, respectively. The second variation mode of H-TESSEL's TB error explains 8 % (horizontal polarization) and 12 % (vertical polarization) of the total variance, which are slightly higher than the percentages obtained for ORCHIDEE's TB error. The pattern correspondent to the horizontal polarization shows that the error is maximum over the South-Western region of the IP, while the vertical polarization one does not show a clear structure. Contrary to the first variation mode, patterns from the second variation mode show larger differences with the ones depicted by the TB error of ORCHIDEE.

The temporal evolution of each variation mode is given by the Expansion Coefficients (ECs). Those corresponding to the first mode of both TB errors are represented in Fig. 5. The four temporal series show a strong annual variation that peaks at Fall. High peaks are also observed in December 2012 and during the Winter 2010–2011, being the error maximum in this season too. Positive ECs imply that there is no sign change in the spatial patterns. So, modelled TBs are warmer than measured ones over the main structure detected in Figs. 3 and 4 (a and c) during these seasons. The behaviour of the ECs coincides with the marked seasonality observed in Fig. 2 for the spatial correlation, and shows that the largest spatially coherent error varies slowly. It is, therefore, dominated by the slow varying component of the TB signals, which is given by their annual cycle. This is contrary to the temporal correlation analysis, which is driven by their synoptic variability. Therefore, the slow and fast varying components of TBs show different behaviours. Both sets of modelled TBs provide similar error structures regarding their annual cycle, but slight differences are detected between the temporal correlations of TB_{HT} and TB_{OR} with TB_{SM}. Dissimilar spatial patterns have been found for the second EOF variation modes. Therefore, their ECs have not been

HESSD
12, 13019–13067, 2015

included in Fig. 5, despite the fact that they showed variations at higher frequency than those from the first modes.

Since the EOF analysis pointed at warmer modelled TBs than TB_{SM} over the South-West of the IP during Fall and Winter, we looked at ECMWF's mean first guess departure from the months of November 2010 to 2012. It consists of the time averaged geographical mean of the difference between measured (SMOS) and modelled (H-TESSEL and CMEM) TBs and is represented in Fig. 6 for both polarizations. The three years show a contrast between the error over the North-Western region of the IP (in an orange colour) and over the South-Western region and a smaller area further North (in a blue colour). According to this, observed TBs are warmer than modelled ones over the North-West of the IP during these periods, while modelled TBs are warmer than SMOS's over the South-West of the IP. This is in good agreement with the behaviour described by the first EOF variation mode of both TB errors (Figs. 3a and c and 4a and c). It should be noted that the TB error occurs at a wider scale. In fact, it is a global bias. However, only the Iberian Peninsula is represented in this figure to show clearly the spatial structures.

Summarizing, the first EOF variation mode shows a spatial structure which appears in the TB error of both models and polarizations. In addition, the temporal evolution of the ECs also coincides between both errors. Therefore, we have identified a dominant structure in the error between modelled and measured TBs, which is maximum in the Fall and Winter seasons, over the South-West of the IP and a smaller area further North. It represents between 18 and 36 % of the error depending on the modelled TB set considered and its polarization.

The common feature of the presented model simulations is the forcing data used. Our first objective is, therefore, to verify that the TB error patterns found are not related to biases in the imposed atmospheric condition. On the one hand, we will focus on the Precipitation (P) and the radiative balance. According to Zollina et al. (2004) precipitation generated by a reanalysis (like ERA-Interim) is highly model dependent, and one of the less reliable forecast parameters since models lack the sufficient skill to

HESSD
12, 13019–13067, 2015

represent accurately all the physical processes that take place in the atmospheric water cycle. We would like to draw the reader's attention to the fact that precipitation has an important effect on the state of the SSM and thus, on emissivity. On the other hand, the available energy at the surface is one of the major drivers of errors in modelled land surface temperature. LST is a key variable to study because it provides a good summary of the surface energy balance, as well as being a key parameter in the TB estimation through CMEM. In addition, modelled LST is affected by a bias with a strong annual cycle and the temporal characterization of the TB error showed a strong annual variation.

It has been decided to look at the dominant pattern of the precipitation and the LST errors. For this matter, further EOF analyses are done to compare them with the EOF performed for the two TB errors. If similarities are identified, we will be able to relate these variables to the spatial inconsistency found in TBs. It should be noted that each one of these analyses approaches the study of the TB error's dominant structure through the TB's main components: emissivity, driven by the hydrological cycle at the surface, and temperature, driven by the thermodynamics of the surface.

3.2.2 LST and precipitation errors

The precipitation error is calculated as the difference between the *P* provided by the ERA-Interim forcing and by the E-OBS independent dataset (Haylock et al., 2008). Two LST errors are computed as the difference between modelled (from ORCHIDEE or H-TESSEL) and measured data. The reference for land surface temperature is chosen to be the one provided by the LandSAF product (http://landsaf.meteo.pt).

The spatial patterns of the *P* and LST errors' first variation mode are represented in Fig. 7, together with their explained variance. We can identify certain structures in the patterns from the LST errors, which differ between the two models. A North–South gradient is observed in the error using ORCHIDEE's LST (Fig. 7a). This structure is most likely explained by forcing induced biases, due to available energy, affecting the LSM simulation. However, the error computed with H-TESSEL's LST (Fig. 7c) shows a gra-

HESSD
12, 13019–13067, 2015

dient from East to West. A different structure is shown by the pattern corresponding to the *P* error (Fig. 7b), where the error is found to be maximum over the South of the peninsula. The temporal evolution of each of these patterns is shown in Fig. 8. It can be seen how the ECs from the *P* error have a higher frequency variation than the ECs computed for the LST errors. ORCHIDEE's LST error behaves as expected from land-surface physics, since the ECs show a maximum in Summer when the largest amount of energy is absorbed by the surface. However, this is not the case for H-TESSEL's LST error, whose ECs show higher frequency variation with maxima in the Fall season and at the end of the Winter in 2011 and 2012.

The comparison of the dominant structure identified in both TB errors with the ones obtained for the precipitation and LST errors, shows mismatches in the spatial patterns (Figs. 3a and c and 4a and c vs. Fig. 7). Furthermore, there is no accordance either between their ECs (Fig. 5 vs. Fig. 8). The TB error's temporal evolution of the spatial patterns showed a strong annual variation which peaked in Fall and Winter. However, the ECs of ORCHIDEE's LST error show a maximum in a different season and those from H-TESSEL's LST and *P* errors are characterized by higher frequency variation. Therefore, forcing biases can be discarded as the main cause of the inconsistency in TB's spatial structures.

After analysing the forcing, the second objective would be to study whether the LSMs are the responsible of the dominant structure identified in the TB error. Models must deal with complex processes regarding the water and energy balances. For this matter, the two LSMs selected here use different approaches, which are unlikely to produce the same systematic errors in the modelling process. However, the two different sets of modelled TBs provide the same dominant structure in the EOF analysis of the TB error which furthermore, is not reflected in the LST biases. Consequently, models are not likely to be the main cause of the inconsistency found between modelled and measured TBs.

The next candidate to explain the TB error is the RTM used to model brightness temperatures: the CMEM, which is also shared by both sets of modelled TBs. In fact,

HESSD
12, 13019–13067, 2015

modelled TBs have been shown to be more sensitive to the configuration of the microwave model than to LSMs (de Rosnay et al., 2009). Focus is put on the configurations defined, and further simulations with the CMEM are carried out to test if assumptions made in the parametrizations used could affect the resulting TBs. One of the parametrizations that the user can define is the vegetation cover input data. Since this parameter is directly related to land-surface emissivity, the effects of a different vegetation cover are tested on TB_{HT}. For this matter, a new set of TBs is modelled using H-TESSEL's state variables with the same configuration as detailed in Table 1, except for the vegetation cover input, where H-TESSEL's prescribed vegetation (Boussetta et al., 2013) is considered. One of the differences between this input and the ECOCLIMAP database, used in this study, is that the former consists of 20 vegetation types, while in the latter these are reduced to 7. The new TB_{HT} set using H-TESSEL's prescribed vegetation provides similar mean spatial correlations with TB_{SM} (0.17 and 0.36 for the horizontal and vertical polarization, respectively) as the ones shown in Table 4 for TB_{HT} and TB_{SM}. In addition, an EOF analysis of the difference between this new set and observed TBs (figure not included) showed similar spatial patterns as the ones identified in Fig. 4a and c, as well as a good agreement between their temporal evolution. Whether or not a coarser soil discretization has an effect on modelled TBs is also tested by recomputing TB_{OR} using ORCHIDEE's state variables averaged to 3 soil layers: upper (9 cm), medium (66 cm), and lower (125 cm). No significant difference is observed between this TB set and the former one when compared to TB_{SM}. For instance, mean spatial correlations are 0.22 and 0.33 for the horizontal and vertical polarization, respectively, which are similar to those shown in Table 4. In addition, the effect of using the Fresnel law to compute ε_s, rather than the parametrization proposed by Wilheit (1978), and Wigneron (2001) to calculate the T_{eff}, instead of using the soil temperature profile, is tested in the estimation of TB_{OR}. An EOF analysis of the TB error computed using the TB_{OR} set with the modified configuration (figure not included), shows a similar dominant structure both in space and time to the one observed in Fig. 3a and c. Therefore, the vegetation cover used, the number of soil layers, and the

HESSD
12, 13019–13067, 2015

above mentioned parametrizations to compute ε_s and T_{eff} are rejected as being the main factors responsible for the inconsistency found in the TB comparison.

Even though these tests do not provide an explanation for the dominant pattern of the TB error, we believe that further analysis concerning CMEM's configuration should be carried out. Especially regarding the way the emissivity estimation is approached in it. This will be discussed in Sect. 4.

3.3 Annual cycle of brightness temperatures

The slow varying component of the TB signals is analysed pixel by pixel over the IP in order to study the annual variation shown in Fig. 5. For this matter, the mean annual cycle of each TB signal is computed. Next, they are smoothed using a spline filter to remove sub-monthly fluctuations, because the study period considered is rather short. We then compute their amplitudes and normalize them by their mean value. These are represented in Fig. 9. The spatial structures shown in SMOS's maps (Fig. 9c and f) coincide with the ones observed in the TB error patterns of the first EOF variation mode (Figs. 3a and c and 4a and c). However, this structure is not found in the maps corresponding to TB_{OR} and TB_{HT}, where there is less contrast in the spatial distribution of the relative amplitude of the annual cycle. CMEM does not seem to reproduce the amplitude of TBs observed by SMOS, which are larger than modelled ones, especially over the area highlighted by the first EOF variation mode of the TB error.

To further analyse this result, two study areas are defined, one over the South-Western region (7.5–4° W, 40–38° N) of the Iberian Peninsula and another one over the North-Western region (8.25–6° W, 43–41.75° N). The former is selected because it corresponds to part of the area where the dominant structure of the TB error has been identified. The North-Western region is chosen because it shows an opposite error to the one observed over the South-West of the IP.

Figure 10 shows the smoothed annual cycle of the horizontal and vertical polarizations of the TB signals from both regions, as well as a map with the exact location of each area. The LST from the LandSAF product as well as those modelled by OR-

HESSD
12, 13019–13067, 2015

CHIDEE and H-TESSEL have also been included in the figure because of their direct relation to TBs. The plot corresponding to the South-Western area shows that, in general, modelled TBs are closer together than with measured TBs. However, it should be noted that TB_{OR} is closer to TB_{SM} than to TB_{HT} during Summer. Models also provide higher values than TB_{SM} throughout the year, meaning that they are warmer than observations over this area. A clear difference can be established between the Summer and Winter seasons, since modelled and measured TBs are closer in the former than in the latter. For instance, the mean difference in Summer between the horizontal polarization of TB_{OR} and TB_{SM} is lower than 1 K, while in Winter it is around 27 K. As for the mean difference between TB_{HT} and TB_{SM}, it is lower than 4 K in Summer and higher than 15 K in Winter. A similar situation is observed for the vertical polarization, where the mean differences between modelled and measured data are lower than 4 K in Summer, and 23 K (TB_{SM} vs. TB_{OR}) and 14 K (TB_{SM} vs. TB_{HT}) in Winter. Therefore, there seems to be a systematic bias between modelled and measured data during the Winter season in the South-Western region. This is in agreement with the EOF analysis shown in Figs. 3a and c, 4a and c, and 5, where the dominant TB error structure, detected over the South-West of the IP, is found to be maximum in Fall and Winter. In addition, we measured a strong difference in the smoothed annual cycle's variance between models and observations during Winter and Summer. For example, if the horizontal polarization is considered, variances from modelled and measured data differ in less than 20 K in Summer and in more than 50 K in Winter. This could be attributed to different mean states of TBs. However, no distinguishable relation between these and the variances has been found. This behaviour explains the poor spatial correlations between modelled and measured TBs during Winter, shown in Fig. 2.

A different behaviour is observed over the North-Western region, where no systematic bias is detected between TBs from models and observations. Actually, measurements are within the modelled TB range during most of the year. It should be noted that, in Summer, measured TBs are higher than modelled ones if the horizontal polarization is considered, while they are in good agreement with TB_{HT}, and especially with

HESSD
12, 13019–13067, 2015

TB_{OR} regarding the vertical polarization. In fact, TB_{SM} is closer to TB_{OR} than to TB_{HT}, which shows lower values than the other two TB signals, throughout the year.

The fact that the behaviour of TB's annual cycle over the South-Western region differs from the one observed over the North-West means that the processes responsible for the TB error are probably different in each region. Over the South-West there is low presence of vegetation and the precipitation events are spread out over the year with large drying periods between them. This results in strong variations of soil moisture over this region. On the other hand, the North-Western region is characterized by an oceanic climate and thus, wet Winters and mild Summers, with a high precipitation, and often rainfall occurring as drizzle. Opposite to the Southern region, there is more vegetation and thus, more biomass in the soil increasing its capacity to retain water and capture the humidity. Therefore, rainfall usually takes place over a wet soil in the North-Western region. It should be noted that rainfall interception plays a greater role over this area than over the South-West of the IP. Since it represents the retention of rainwater by the plant cover, it is directly related to the vegetation water content which has a strong influence on TBs (Jones et al., 2004). Consequently, differences between modelled and measured TBs shown in Fig. 10b could be explained by assumptions made in the modelling approach used for this process. However, it should be recalled that the error over the South-West of the IP is prevalent, as shown by the EOF analysis.

The smoothed annual cycle of the LST modelled by ORCHIDEE and the one provided by the LandSAF product are in good agreement over both regions. The South-West plot shows that the error between the two datasets is maximum in Summer, contrary to the TB error, which is maximum in Winter. On the other hand, the annual cycle of H-TESSEL's modelled LST, shows larger amplitudes and warmer temperatures than those observed for ORCHIDEE and LandSAF's LST. Therefore, if the LST was the main responsible for the TB error, TB_{HT} would be expected to be higher than TB_{SM} over the North-Western region in Winter, which is the opposite of the actual behaviour. These results confirm our hypothesis of rejecting forcing induced biases affecting the modelling of processes related to temperature as the main responsible for the spatial

HESSD
12, 13019–13067, 2015

inconsistency found in the TB comparison. Analysing the difference found between the annual cycles of H-TESSEL's LST signal and the other two LST signals, is beyond the scope of this paper.

4 Discussion and conclusions

This study complements a previous one where modelled Surface Soil Moisture (SSM) from the ORCHIDEE Land Surface Model (LSM) was compared to retrieved SSM from SMOS (Polcher et al., 2015). The spatial structures of modelled SSM were found to be inconsistent with those from retrieved SSM. Since Brightness Temperatures (TBs) are the main input in the soil moisture retrieval algorithm, a comparison between measured and modelled TBs would help to better understand this inconsistency. For this matter, TBs of SMOS's Level 1C product were compared to two sets of modelled TBs. The latter were obtained using LSM-simulated state variables (from the ORCHIDEE and H-TESSEL LSMs) and a radiative transfer model, CMEM. The study was carried out over the Iberian Peninsula (IP) for the period 2010 to 2012.

After computing the temporal correlation between measured and modelled TBs, it was concluded that there is a good agreement in their temporal evolution. On the other hand, a large mismatch was detected between the TB spatial structures provided by models and observations. Similar conclusions were obtained in the comparison between retrieved and modelled SSM. It should be noted that this study found that the temporal correlation of SSM was mainly driven by its synoptic variability and thus, there is a lack of information regarding its annual cycle when this methodology is used.

The error between modelled and measured TBs was characterized spatially and temporally by means of an EOF analysis. First, a dominant structure over the South-Western region of the Iberian Peninsula and a smaller area further North, which evolves during the year and is maximum in Fall and Winter, was detected using both sets of modelled TBs. Therefore, the inconsistency is not limited to a particular LSM. This behaviour differs from the error characterization of the SSM comparison, which

HESSD
12, 13019–13067, 2015

showed the largest discrepancies between modelled and retrieved SSM over the North-Western region of the IP. In fact, only weak differences were found over the South-Western region (Polcher et al., 2015). This suggests that the TB error seems to be compensated by the soil moisture retrieval algorithm used in the SMOS processing chain which produces the L2 product. Secondly, the structure identified for the difference between modelled and measured brightness temperatures explains between 18 and 36 % of the variance of the TB error, depending on the set of modelled TB and polarization considered. So there is a high percentage of the error that shows structures which have to be analysed and explained. Since these are not present in both LSMs, they are of lower priority and have not been approached in this study. Finally, the smoothed annual cycle of observed TBs shows, generally, larger amplitudes than simulated TBs. A more specific analysis of the annual cycle's amplitude performed over a region located at the South-West of the IP showed that models are warmer than observations and allowed to identify a systematic bias between measured and modelled TBs in Winter.

Since the two sets of modelled TBs used in this study provided the same dominant TB error structure, focus was put on their common features in order to try to understand the origin of this inconsistency. These are the forcing data used to perform the ORCHIDEE and H-TESSEL simulations, and the radiative transfer model used to simulate TBs (CMEM).

In the first place, we studied whether forcing induced biases could have an impact on modelled TBs. For this, further EOF analyses were performed for the errors of the Precipitation (P) and the Land Surface Temperature (LST). This study aimed at comparing the dominant error structures obtained for P and LST with those from the EOF analysis carried out for the TB error to try and identify similarities. However, dissimilar spatial patterns and expansion coefficients were found, implying that biases in the forcing are not the dominant factor in the error between modelled and measured TBs. Nevertheless, it should be noted that the degree of accuracy of the forcing can not be fully established because of scale issues and the lack of sufficient independent measure-

HESSD
12, 13019–13067, 2015

ments. The difference in TBs' spatial structures could also be thought of a combination of non linear relations between errors in P and LST, but this is beyond the scope of this paper.

In the second place, we analysed if the differences between modelled and measured TBs could be explained by assumptions made in the parametrizations selected in CMEM's configuration. To do so, modelled TBs were recomputed with variations in the configurations previously defined. First, the effect of vegetation was analysed by computing TBs with H-TESSEL's state variables and a different vegetation cover input. Secondly, TBs were modelled using ORCHIDEE's state variables with the soil temperature and moisture profiles averaged to 3 layers to test the effect of a coarser soil discretization. Finally, the effects of the parametrization of Wilheit (1978) to compute the smooth surface emissivity, and of the use of the soil temperature profile for the effective temperature were also analysed. For this matter, ORCHIDEE's TBs were modelled using a different parametrization for these variables. In all of the cases, a similar error structure was obtained for the difference between modelled and measured TBs as the original one. Therefore, none of these tests identified a candidate for explaining a large fraction of the TB error. However, we believe that further analysis should be carried out in this direction. In our opinion, the main spatial structure identified in both TB errors and the fact that it is dominated by the brightness temperature's annual cycle suggests that it contains a geophysical signal. Since the emissivity is directly related to TBs, we propose to concentrate on assumptions made in CMEM to compute this parameter (or others related to it) and how they impact TB's spatial structures.

According to Jones et al. (2004), the soil moisture and vegetation water content have a significant effect on the sensitivity of TB at the top of the atmosphere. However, they impact microwave emission in different ways. On the one hand, an increase in soil moisture results in a higher soil dielectric constant (ϵ) and thus, on lower emissivities. On the other hand, an increase in the vegetation water content rises the scatter and the absorption, increasing the emission. The ϵ is key in the computation of emissivity, while the vegetation optical depth (τ_{veg}) is closely related to the vegetation water

HESSD
12, 13019–13067, 2015

content. Both of these variables are modelled in CMEM and the same parametrization has been used for the two sets of modelled TBs: Wang and Schmugge (1980) for ϵ and Wigneron et al. (2007) for τ_{veg}. Furthermore, the same parametrization has been used to model the rough surface emissivity (ε_r) in both sets too: Wigneron et al. (2001). Considering that similar spatial patterns were obtained for the TB error using two different sets of modelled TBs, focus should be put on the above mentioned variables (ϵ, τ_{veg}, and ε_r). We propose to analyse the relation between the vegetation water content and TB in the first place. The reason being that the vegetation opacity model plays an important role in modelled TB's sensitivity to CMEM's configuration, as shown in de Rosnay et al. (2009). In addition, we should recall that no significant differences were observed between modelled and retrieved surface soil moisture (related to ϵ) over the region where the maximum of the TB error was identified.

Deficiencies or missing processes in both LSMs can also be envisaged as causes to explain the inconsistency found in TB's spatial structures. In fact, the analysis discussed above would also imply to revise certain processes from the LSMs. For instance, the rainfall interception, which according to Wigneron et al. (2007) has a significant effect on τ_{veg}, or the Leaf Area Index (LAI), which is a key component in the CMEM parametrization of τ_{veg}. It would be interesting to study this variable, as it is linked to the seasonal cycle of vegetation and it may reveal some underestimated effects of vegetation dynamics on modelled TBs. The fact that the attenuation effect of litter on the soil is not taken into account by models, but is observed by satellites, could also explain differences obtained between modelled and measured TBs. However, we think that probably it would not cause such an impact as the one observed over the South-Western area of the Iberian Peninsula without affecting other regions too. Finally, issues related to the fundamental characteristics of the LSMs may also explain the inconsistency between the spatial structures of modelled and measured TBs. For instance, LSMs do not represent small scales, at which heterogeneity in topography, soil, and vegetation normally occurs. Assumptions made by LSMs could neglect key issues from the small scale which could be carried over to the large scales of TBs.

HESSD
12, 13019–13067, 2015

According to Entin et al. (2000), the temporal and spatial variability of soil moisture can be separated into a small and a large scale. The former is related to land surface characteristics (soil properties, vegetation, rooting system, etc.), while the large scale deals with atmospheric processes, like evaporation and precipitation. For instance, in Cayan and Georgakakos (1995) SM large-scale coherence is connected to potential evaporation and precipitation. A better knowledge of these scales is key for climate modelling since: (i) it provides information about the percentage of SM variation explained by each scale and thus by short and long-term influences, (ii) it can improve the representation of how a SM change in one point affects the area surrounding it, and (iii) help in the model spatial grid size and time step determination.

Instrumental issues from SMOS could also explain part of the TB differences in spatial structures, in case these are not of climatological or geophysical nature. For example, one of the most important causes of noise in SMOS's surface soil moisture are Radio-Frequency Interferences (RFIs). Daganzo-Eusebio et al. (2013) describe their effect on SMOS's data. Some of them are difficult to detect and thus, RFIs may not be properly filtered out. For instance, Dente et al. (2012) identified an irregular angular pattern in the TBs affecting data from the L1C product used to retrieve soil moisture. In their opinion, this was caused by weak RFIs which were not correctly filtered. Another explanation could be antenna pattern errors, as SMOS's TBs seasonal and latitudinal drifts detailed in Oliva et al. (2013).

In previous studies, differences between the spatial structures of modelled and retrieved surface soil moisture were found (Parrens et al., 2012; Polcher et al., 2015). Results from this paper show that these structures are not consistent either when comparing modelled and observed brightness temperatures. It should be recalled that although the study here presented is limited to the Iberian Peninsula, differences in spatial structures occur at a global scale. We would like to draw the reader's attention to the fact that TBs are not only the main input of SMOS's soil moisture retrieval algorithm, but that they are used to retrieve other variables, like vegetation optical depth or salinity. We believe that analysing the spatial structures of modelled and measured TBs

HESSD
12, 13019–13067, 2015

and understanding the inconsistencies between them is an important issue as it can affect geophysical estimates, TB assimilation in operational models, as well as result in misleading validation studies. Therefore, obtaining the spatial contrast of observed TBs in models is a challenge which, in our opinion, should be approached from a modelling and an observational point of view.

Acknowledgements. The authors would like to thank the helpful comments of Filipe Aires and Jean-Pierre Wigneron. This work contributes to the FP7 Earth2Observe project under grant agreement No. 603608.

References

Albergel, C., Zakharova, E., Calvet, J. C., Zribi, M., Pardé, M., Wigneron, J. P., Novello, N., Kerr, Y., Mialon, A., and Fritz, N.: A first assessment of the SMOS data in southwestern France using in situ and airborne soil moisture estimates: the CAROLS airborne campaign, Remote Sens. Environ., 115, 2718–2728, 2011.

Balsamo, G., Vitterbo, P., Beljaars, A., van den Hurk, B., Hirschi, M., Betts, A. K., and Scipal, K.: A revised hydrology for the ECMWF model: verification from field site to terrestrial water storage and impact in the integrated forecast system, J. Hydrometeorol., 10, 623–643, doi:10.1175/2008JHM1068.1, 2009.

Bircher, S., Skou, N., and Kerr, Y.: Validation of SMOS L1C and L2 products and important parameters of the retrieval algorithm in the Skjern river catchment, Western Denmark, IEEE T. Geosci. Remote Sens., 51, 2969–2985, doi:10.1109/TGRS.2012.2215041, 2013.

Björnsson, H. and Venegas, S. A.: A Manual for EOF and SVD Analyses of Climatic Data, Report No. 97-1, Department of Atmospheric and Oceanic Sciences and Centre for Climate and Global Change Research, McGill University, Montréal, Canada, 52 pp., 1997.

Bousseta, S., Balsamo, G., Beljaars, A., Kral, T., and Jarlan, L.: Impact of a satellite-derived leaf area index monthly climatology in a global numerical weather prediction model, Int. J. Remote Sens., 34, 3520–3542, doi:10.1080/01431161.2012.716543, 2013.

Cayan, D. R. and Georgakakos, K. P.: Hydroclimatology of continental watersheds, 2. Spatial analyses, Water Resour. Res., 31, 677–697, doi:10.1029/94WR02376, 1995.

HESSD

12, 13019–13067, 2015

Daganzo-Eusebio, E., Oliva, R., Kerr, Y., Nieto, S., Richaume, P., and Mecklenburg, S.: SMOS radiometer in the 1400–1427 MHz passive band: impact of the RFI environment and approach to its mitigation and cancellation, IEEE T. Geosci. Remote, 51, 4999–5007, 2013.

Dee, D. P., Uppala, S. M., Simmons, A. J., Berrisford, P., Poli, P., Kobayashi, S., and Andrae, U.: The ERA-interim reanalysis: configuration and performance of the data assimilation system, Q. J. Roy. Meteorol. Soc., 137, 553–597, doi:10.1002/qj.828, 2011.

Dente, L., Su, Z., and Wen, J.: Validation of SMOS soil moisture products over the Maqu and Twente regions, Sensors, 12, 9965–9986, doi:10.3390/s120809965, 2012.

de Rosnay, P. and Polcher, J.: Modelling root water uptake in a complex land surface scheme coupled to a GCM, Hydrol. Earth Syst. Sci., 2, 239–255, doi:10.5194/hess-2-239-1998, 1998.

De Rosnay, P., Drusch, M., Boone, A., Balsamo, G., Decharme, B., Harris, P., Kerr, Y., Pellarin, T., Polcher, J., and Wigneron, J. P.: The AMMA Land Surface Model intercomparison experiment coupled to the Community Microwave Emission Model: ALMIP-MEM, J. Geophys. Res., 114, D05108, doi:10.1029/2008JD010724, 2009.

d'Orgeval, T., Polcher, J., and de Rosnay, P.: Sensitivity of the West African hydrological cycle in ORCHIDEE to infiltration processes, Hydrol. Earth Syst. Sci., 12, 1387–1401, doi:10.5194/hess-12-1387-2008, 2008.

Drusch, M., Wood, E. F., and Jackson, T.: Vegetative and atmospheric corrections for soil moisture retrieval from passive microwave remote sensing data: results from the Southern Great Plains hydrology experiment 1997, J. Hydrometeorol., 2, 181–192, 2001.

Entekhabi, D., Njoku, E. G., O'Neill, P. E., Kellogg, K. H., Crow, W. T., Edelstein, W. N., Entin, J. K., Goodman, S. D., Jackson, T. J., Johnson, J., Kimball, J., Piepmeier, J. R., Koster, R. D., Martin, N., McDonald, K. C., Moghaddam, M., Moran, S., Reichle, R., Shi, J. C., Spencer, M. W., Thurman, S. W., Tsang, L., and Van Zyl, J.: The Soil Moisture Active Passive (SMAP) mission, Proc. IEEE, 98, 704–716, 2010.

Entin, J. K., Robock, A., Vinnikov, K. Y., Hollinger, S. E., Liu, S., and Namkhai, A.: Temporal and spatial scales of observed soil moisture variations in the extratropics, J. Geophys. Res., 105, 11865–11877, doi:10.1029/2000JD900051, 2000.

Escorihuela, M. J., Chanzy, A., Wigneron, J. P., and Kerr, Y.: Effective soil moisture sampling depth of L-band radiometry: a ase study, Remote Sens. Environ., 114, 995–1001, doi:10.1016/j.rse.2009.12.011, 2010.

HESSD
12, 13019–13067, 2015

González-Zamora, A., Sánchez, N., Martínez-Fernández, J., Gumuzzio, A., Piles, M., and Olmedo, E.: Long-term SMOS soil moisture products: A comprehensive evaluation across scales and methods in the Duero Basin (Spain), Phys. Chem. Earth Parts A/B/C, 83–84, 123–136, doi:10.1016/j.pce.2015.05.009, 2015.

Green, W. H. and Ampt, G.: Studies on soil physics, 1. the flow of air and water through soils, J. Agr. Sci., 4, 1–24, 1911.

Haylock, M. R., Hofstra, N., Klein Tank, A. M. G., Klok, E. J., Jones, P. D., and New, M.: A European daily high-resolution gridded dataset of surface temperature and precipitation, J. Geophys. Res.-Atmos., 113, D20119, doi:10.1029/2008JD010201, 2008.

Holmes, T. R. H., Jackson, T. J., Reichle, R. H., and Basara, J. B.: An assessment of surface soil temperature products from numerical weather prediction models using ground-based measurements, Water Resour. Res., 48, W02531, doi:10.1029/2011WR010538, 2012.

Jones, A., Vukićević, T., and Vonder Haar, T.: A microwave satellite observational operator for variational data assimilation of soil moisture, J. Hydrometeorol., 5, 213–229, 2004.

Kanamitsu, M., Yoshimura, K., Yhang, Y. B., and Hong, S. Y.: Errors of interannual variability and trend in dynamical downscaling of reanalysis, J. Geophys. Res., 115, 17115, doi:10.1029/2009JD013511, 2010.

Kerr, Y., Waldteufel, P., Wigneron, J. P., Delwart, S., Cabot, F., Boutin, J., Escorihuela, M., Font, J., Reul, N., Gruhier, C., Juglea, S., Drinkwater, M., Hahne, A., Martin-Neira, M., and Mecklenburg, S.: The SMOS mission: new tool for monitoring key elements of the global water cycle, Proc. IEEE, 98, 666–687, 2010.

Kerr, Y., Waldteufel, P., Richaume, P., Wigneron, J. P., Ferrazzoli, P., Mahmoodi, A., Bitar, A. A., Cabot, F., Gruhier, C., Juglea, S., Leroux, D., Mialon, A., and Delwart, S.: The SMOS soil moisture retrieval algorithm, IEEE T. Geosci. Remote, 50, 1384–1403, 2012.

Kolassa, J., Aires. F., Polcher, J., Pringent, C., Jiménez, C., and Pereira, J. M.: Soil moisture retrieval from multi-instrument observations: information content analysis and retrieval methodology, J. Geophys. Res.-Atmos., 118, 4847–4859, doi:10.1029/2012JD018150, 2013.

Krinner, G. N., Viovy, N., de Noblet-Ducoudré, N., Ogée, J., Polcher, J., Friedlingstein, P., Ciais, P., Stich, S., and Prentice, I. C.: A dynamic global vegetation model for studies of the coupled atmosphere-biosphere system, Global Biogeochem. Cy., 19, GB1015, doi:10.1029/2003GB002199, 2005.

Le Vine, D., Lagerloef, G. S. E., and Torrusio, S.: Aquarius and remote sensing of sea surface salinity from space, Proc. IEEE, 98, 688–703, doi:10.1109/JPROC.2010.2040550, 2010.

HESSD
12, 13019–13067, 2015

Marthews, T. R., Quesada, C. A., Galbraith, D. R., Malhi, Y., Mullins, C. E., Hodnett, M. G., and Dharssi, I.: High-resolution hydraulic parameter maps for surface soils in tropical South America, Geosci. Model Dev., 7, 711–723, doi:10.5194/gmd-7-711-2014, 2014.

Mätzler, C. and Standley, A.: Technical note, relief effects for passive microwave remote sensing, Int. J. Remote Sens., 21, 2403–2412, doi:10.1080/01431160050030538, 2000.

McMullan, K., Brown, M., Martín-Neira, M., Rits, W., Ekholm, S., Marti, J., and Lemanczyck, J.: SMOS: the payload, IEEE T. Geosci. Remote, 46, 594–605, 2008.

Milly, P. C. D.: Potential evaporation and soil moisture in general circulation models, J. Climate, 5, 209–226, 1992.

Montzka, C., Bogena, H., Weihermüller, L., Jonard, F., Dimitrov, M., Bouzinac, C., Kainulainen, J., Balling, J. E., Vanderborght, J., and Vereecken, H.: Radiobrightness validation on different spatial scales during the SMOS validation campaign 2010 in the Rur catchment, Germany, IEEE T. Geosci. Remote, 51, 1728–1743, doi:10.1109/TGRS.2012.2206031, 2013.

Ngo-Duc, T., Polcher, J., and Laval, K.: A 53-year forcing data set for land surface models, J. Geophys. Res., 110, D06116, doi:10.1029/2004JD005434, 2005.

Oliva, R., Martín-Neira, M., Corbella, I., Torres, F., Kainulainen, J., Tenerelli, J., Cabot, F., and Martin-Porqueras, F.: SMOS calibration and instrument performance after one year in orbit, IEEE T. Geosci. Remote, 51, 654–670, 2013.

Parrens, M., Zakharova, E., Lafont, S., Calvet, J.-C., Kerr, Y., Wagner, W., and Wigneron, J.-P.: Comparing soil moisture retrievals from SMOS and ASCAT over France, Hydrol. Earth Syst. Sc., 16, 423–40, doi:10.5194/hess-16-423-2012, 2012.

Parrens, M., Calvet, J.-C., de Rosnay, P., and Decharme, B.: Benchmarking of L-band soil microwave emission models, Remote Sens. Environ., 140, 407–419, doi:10.1016/j.rse.2013.09.017, 2014.

Pellarin, T., Wigneron, J. P., Calvet, J.-C., and Waldteufel, P.: Global soil moisture retrieval from a synthetic L-band brightness temperature data set, J. Geophys. Res.-Atmos., 108, 4364, doi:10.1029/2002JD003086, 2003.

Polcher, J., Piles, M., Gelati, E., Tello, M., and Barella-Ortiz, A.: Comparing upper-soil moisture from SMOS and a land-surface model over the Iberian Peninsula, Remote Sens. Environ., accepted, 2015.

HESSD
12, 13019–13067, 2015

Post, W. M. and Zobler, L.: Global soil types, 0.5-degree Grid (modified zobler), Oak Ridge National Laboratory Distributed Active Archive Center, Oak Ridge, Tennessee, USA, doi:10.3334/ORNLDAAC/540, 2000.
Rüdiger, C., Walker, J. P., Yann, K., Mialon, A., Merlin, O., and Kim, E. J.: Validation of the level 1c and level 2 SMOS products with airborne and ground-based observations, P. Int. Congr. MODSIM, 12–16 December 2011, Perth, Australia, 2011.
Sánchez, N., Martínez-Fernández, J., Scaini, A., and Pérez-Gutiérrez, C.: Validation of the SMOS L2 soil moisture data in the REMEDHUS network (Spain), IEEE T. Geosci. Remote, 50, 1602–1611, doi:10.1109/TGRS.2012.2186971, 2012.
Santaren, D., Peylin, P., Viovy, N., Ciais, P.: Optimizing a process-based ecosystem model with eddy-covariance flux measurements: a pine forest in southern France, Global Biogeochem. Cy., 21, GB2013, doi:10.1029/2006GB002834, 2007.
Schlenz, F., dall'Amico, J. T., Mauser, W., and Loew, A.: Analysis of SMOS brightness temperature and vegetation optical depth data with coupled land surface and radiative transfer models in Southern Germany, Hydrol. Earth Syst. Sci., 16, 3517–3533, doi:10.5194/hess-16-3517-2012, 2012.
Schulz, J. P., Dümenil, L., and Polcher, J.: On the land surface–atmosphere coupling and its impact in a single-column atmospheric model, J. Appl. Meteorol., 40, 642–663, 2001.
Viterbo, P. and Beljaars, A.: An improved land surface parameterization scheme in the ECMWF model and its validation, J. Climate, 8, 2716–2748, 1995.
Wang, J. R. and Schmugge, T.: An empirical model for the complex dielectric permitivity of soils as a function of water content, IEEE T. Geosci. Remote, 18, 288–295, 1980.
Wigneron, J. P., Laguerre, L., and Kerr, H.: A simple parameterization of the L-band microwave emission from rough agricultural soils, IEEE T. Geosci. Remote, 39, 1697–1707, 2001.
Wigneron, J. P., Kerr, Y., Waldteufel, P., Saleh, K., Escorihuela, M., Richaume, P., Ferrazzoli, P., Grant, J. P., Hornbuckle, B., de Rosnay, P., Calvet, J.-C., Pellarin, T., Gurney, R., and Mätzler, C.: L-band microwave emission of the biosphere (L-MEB) model: results from calibration against experimental data sets over crop fields, Remote Sens. Environ., 107, 639–655, 2007.
Wilheit, T. T.: Radiative transfert in plane stratified dielectric, IEEE T. Geosci. Remote, 16, 138–143, 1978.
WWAP – World Water Assessment Programme: The United Nations World Water Development Report 4, Managing Water under Uncertainty and Risk, UNESCO, Paris, France, 2012.

HESSD
12, 13019–13067, 2015

Zollina, O., Kapala, A., Simmer, C., and Gulev, S. K.: Analysis of extreme precipitation over Europe from different reanalyses: a comparative assessment, Global Planet. Change, 44, 129–161, 2004.

HESSD
12, 13019–13067, 2015

Table 1. CMEM configuration for the two sets of modelled TBs.

	Configuration	Parametrization	
		ORCHIDEE	H-TESSEL
Physical configuration	Soil dielectric constant	Wang and Schmugge (1980)	
	Effective temperature	Soil temperature profile	Wigneron et al. (2001)
	Smooth surface emissivity	Wilheit (1978)	Fresnel law
	Rough surface emissivity	Wigneron et al. (2001)	
	Vegetation optical depth	Wigneron et al. (2007)	
	Atmospheric optical depth	Pellarin et al. (2003)	
	Temperature of vegetation	Surface soil temperature	
	Vegetation cover input data	Ecoclimap	
Observing configuration	Microwave frequency	1.4Ghz	
	Incidence angle	42.5°	40°
Soil and atmospheric level configuration	Number of soil layers	11	3
	(number of layers in the top 5 cm)	(5)	(1)

HESSD
12, 13019–13067, 2015

Table 2. Input variables for the CMEM to compute TBs at TOA.

Soil conditions	Constant fields	Soil texture fraction (%) Orography (km)
Vegetation	Constant fields	High and low vegetation types High and low vegetation fractions Water fraction
	Dynamic fields	Low vegetation LAI
Meteorology	Dynamic fields	Soil moisture profile ($m^3\,m^{-3}$) Soil temperature profile (K) Skin temperature (K) Snow depth (m) Snow density ($kg\,m^{-3}$) 2 m temperature (K)

HESSD
12, 13019–13067, 2015

Table 3. TB filtering criteria to keep data, applied to the TB signals.

TB_{OR}	TB_{HT}	All TB signals
ORCHIDEE's daily average surface temperature > 275 K	Snow water equivalent < 0.01 m	Daily TB < 300 K
ERA-Interim's daily average 2 m air temperature > 273 K	ERA-Interim's daily average 2 m air temperature > 273.5 K Orography (slope) < 0.04	Mask (from SMOS's L2 product)

HESSD
12, 13019–13067, 2015

Table 4. Mean temporal and spatial correlations for SSM (Polcher et al., 2015) and the horizontal and vertical polarization of TBs over the Iberian Peninsula from 2010 to 2012.

	Temporal		Spatial	
	Horizontal	Vertical	Horizontal	Vertical
TB_{OR} vs. TB_{SM}	0.75	0.76	0.20	0.30
TB_{HT} vs. TB_{SM}	0.82	0.82	0.24	0.29
SSM_{OR} vs. SSM_{SM}	0.81		0.28	

HESSD
12, 13019–13067, 2015

Table 5. Spatial correlation for the first and second variation modes of the EOF analyses performed for the difference between modelled and measured TBs. TBH and TBV correspond to the horizontal and vertical polarizations, respectively.

	Mode 1	Mode 2
$TB_{OR} - TB_{SM}$ (TBH) vs. $TB_{OR} - TB_{SM}$ (TBV)	0.99	0.97
$TB_{HT} - TB_{SM}$ (TBH) vs. $TB_{HT} - TB_{SM}$ (TBV)	0.86	0.75
$TB_{OR} - TB_{SM}$ (TBH) vs. $TB_{HT} - TB_{SM}$ (TBH)	0.92	0.69
$TB_{OR} - TB_{SM}$ (TBV) vs. $TB_{HT} - TB_{SM}$ (TBV)	0.73	0.48

HESSD
12, 13019–13067, 2015

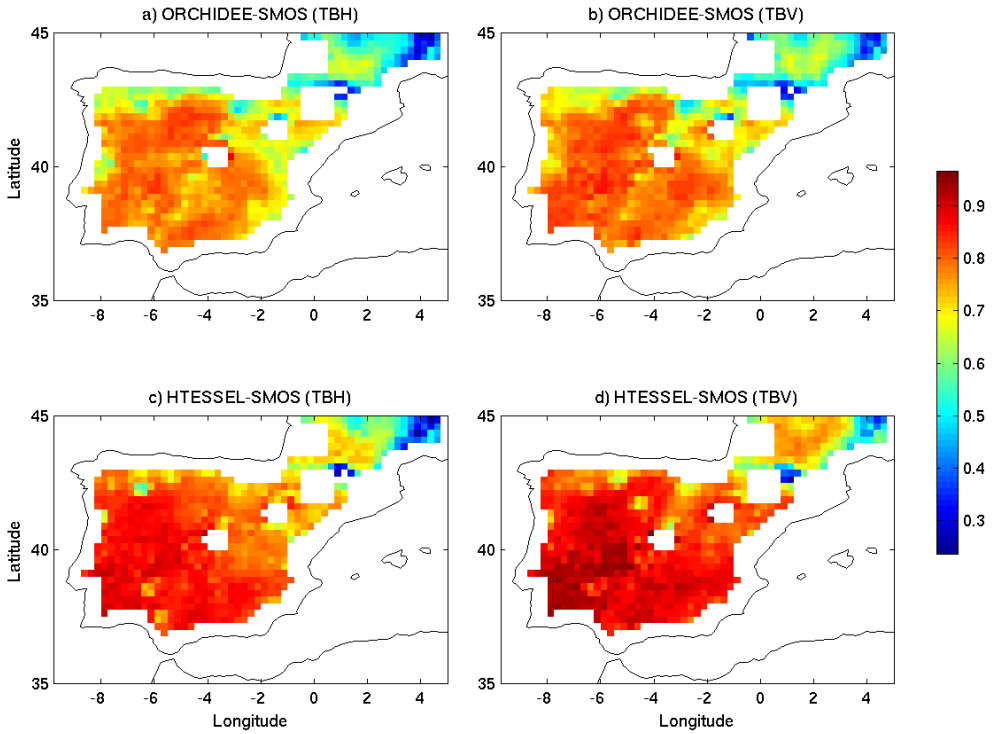

Figure 1. Temporal correlation between modelled and measured TBs from 2010 to 2012. TBH and TBV correspond to the horizontal and vertical polarizations, respectively.

HESSD
12, 13019–13067, 2015

Comparison of measured brightness temperatures from SMOS

A. Barella-Ortiz et al.

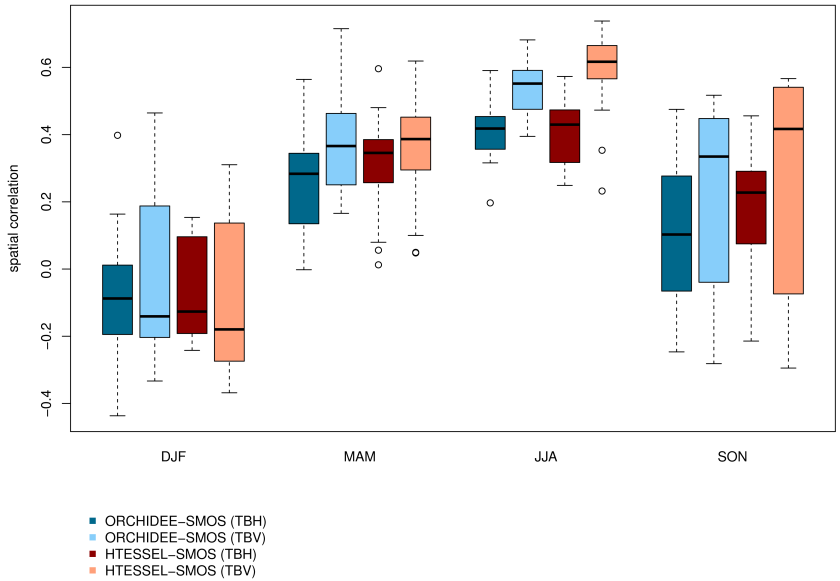

Figure 2. Boxplot showing the annual cycle of the spatial correlation between modelled and measured TBs, over the Iberian Peninsula from 2010 to 2012. TBH and TBV correspond to the horizontal and vertical polarizations, respectively. Values have been grouped per seasons: Winter (DJF), Spring (MAM), Summer (JJA), and Fall (SON).

HESSD
12, 13019–13067, 2015

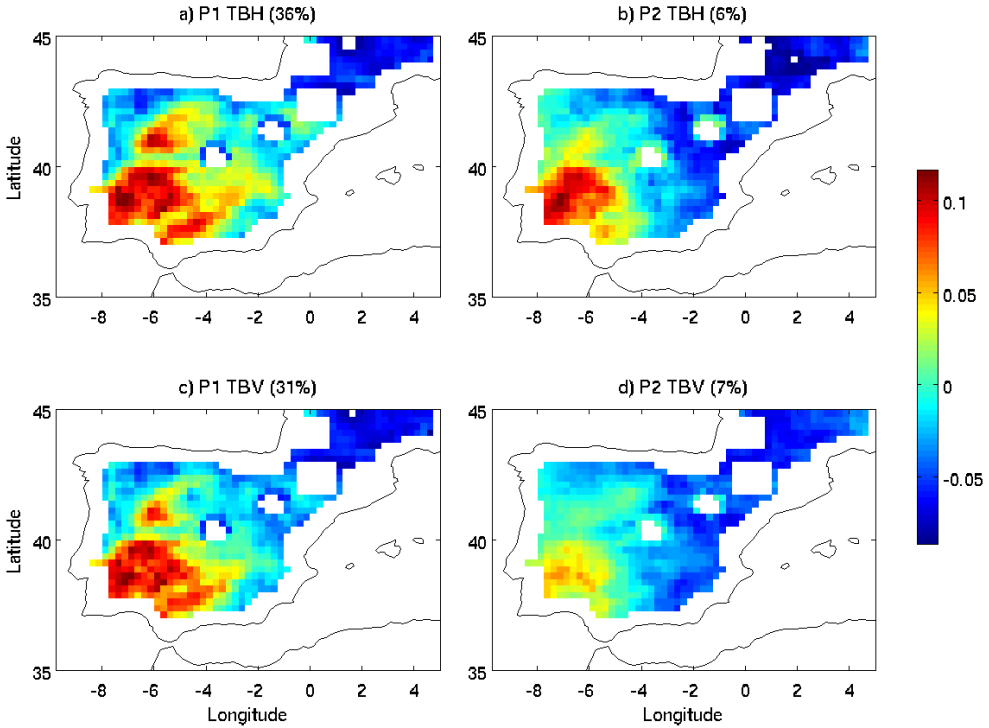

Figure 3. Spatial patterns associated with the first two EOF variation modes (P1 and P2) of the difference between modelled TB (ORCHIDEE) and measured TB (SMOS). TBH and TBV correspond to the horizontal and vertical polarizations, respectively. The percentage of variance explained by each mode is included in brackets.

HESSD
12, 13019–13067, 2015

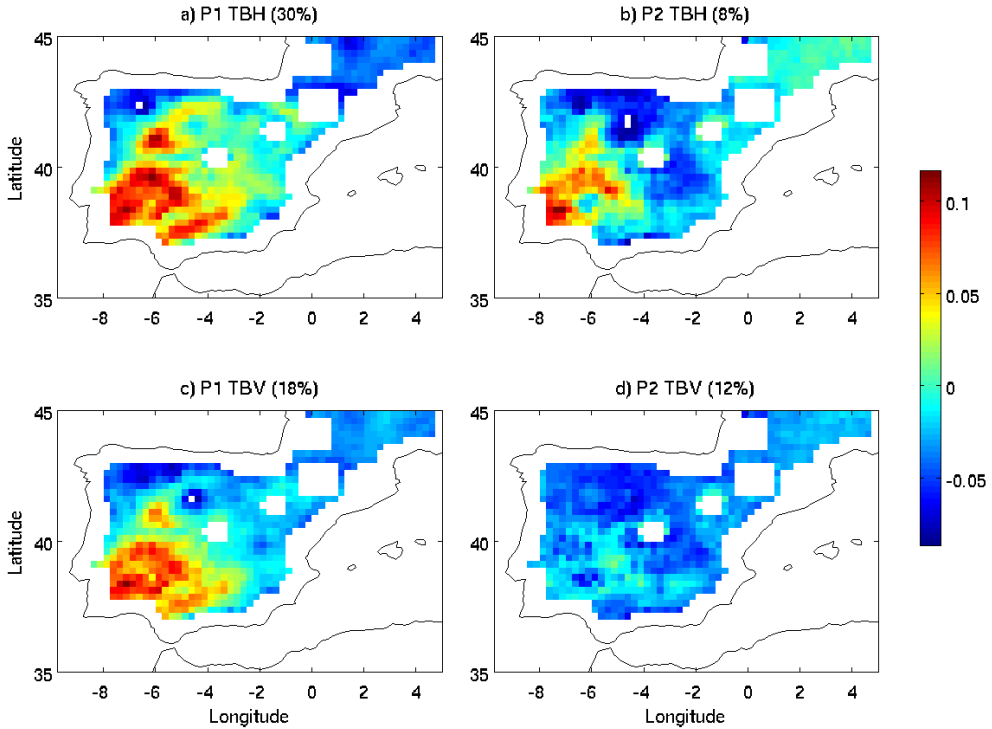

Figure 4. Spatial patterns associated with the first two EOF variation modes (P1 and P2) of the difference between modelled TB (H-TESSEL) and measured TB (SMOS). TBH and TBV correspond to the horizontal and vertical polarizations, respectively. The percentage of variance explained by each mode is included in brackets.

HESSD
12, 13019–13067, 2015

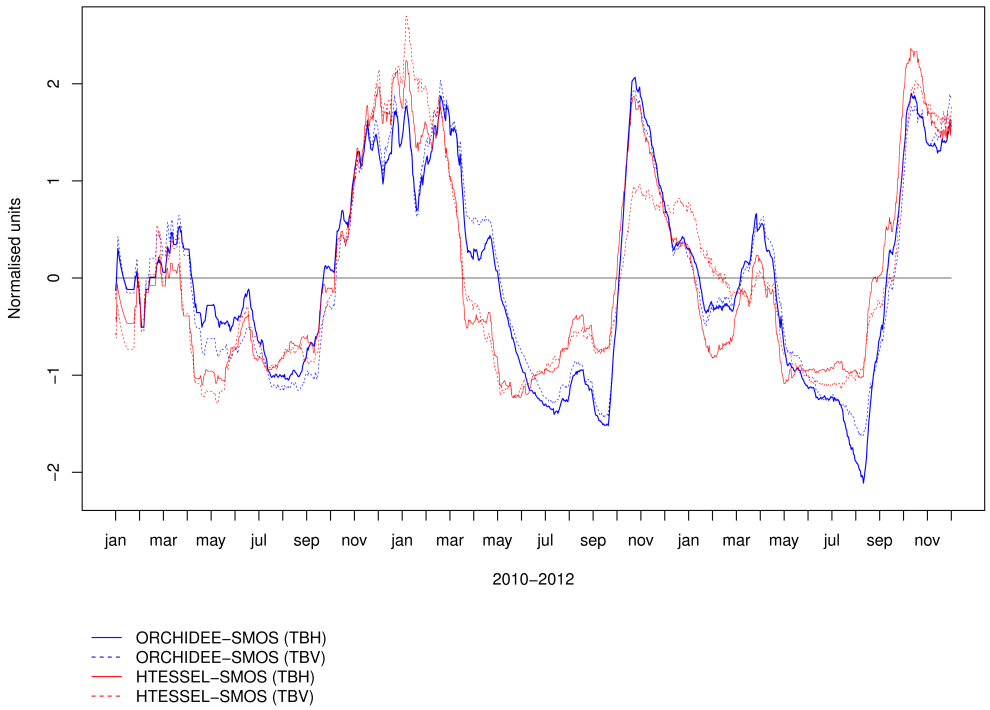

Figure 5. Temporal evolution of the expansion coefficients correspondent to the first EOF variation mode of the TB errors (ORCHIDEE vs. SMOS and H-TESSEL vs. SMOS) over the Iberian Peninsula. Values have been normalized using the standardization method. TBH and TBV correspond to the horizontal and vertical polarizations, respectively.

HESSD
12, 13019–13067, 2015

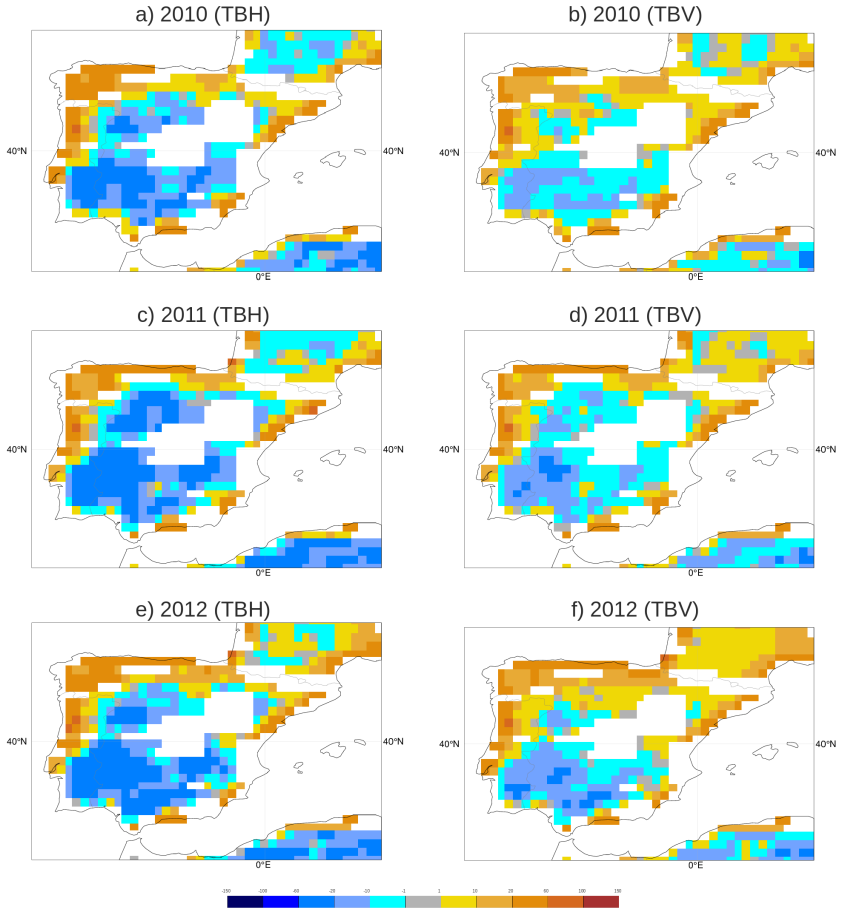

Figure 6. Mean first guess departure (observation-model [K]) from the months of November 2010 to 2012. TBH and TBV correspond to the horizontal and vertical polarizations, respectively.

HESSD
12, 13019–13067, 2015

Comparison of measured brightness temperatures from SMOS

A. Barella-Ortiz et al.

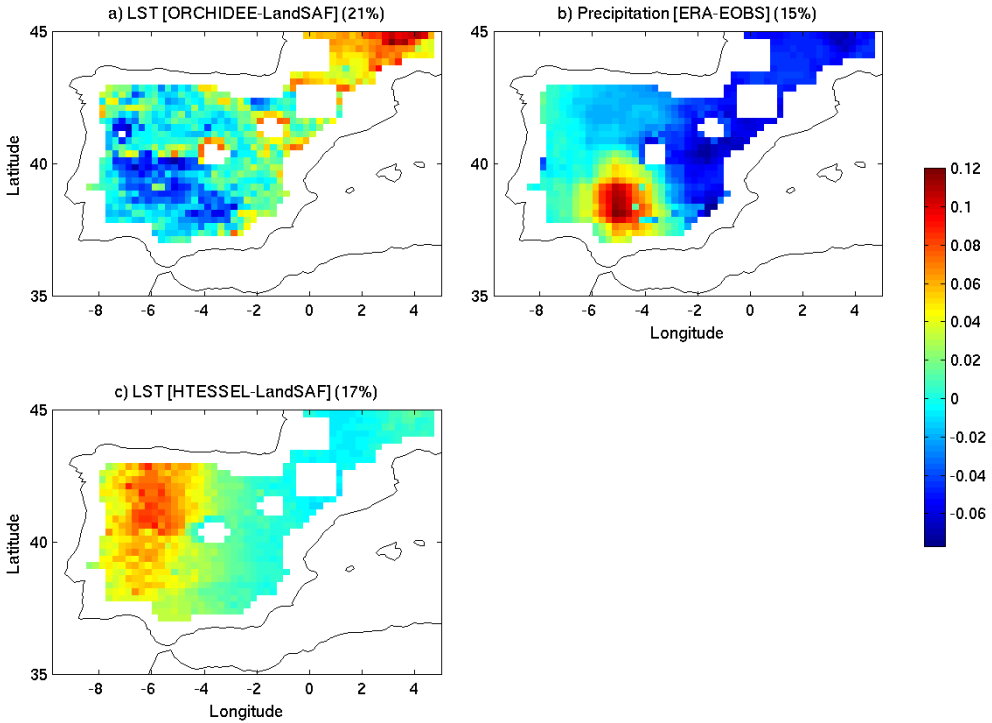

Figure 7. Spatial patterns from the first EOF variation mode of the LST and the precipitation errors. The percentage of variance explained by each mode is included in brackets.

HESSD
12, 13019–13067, 2015

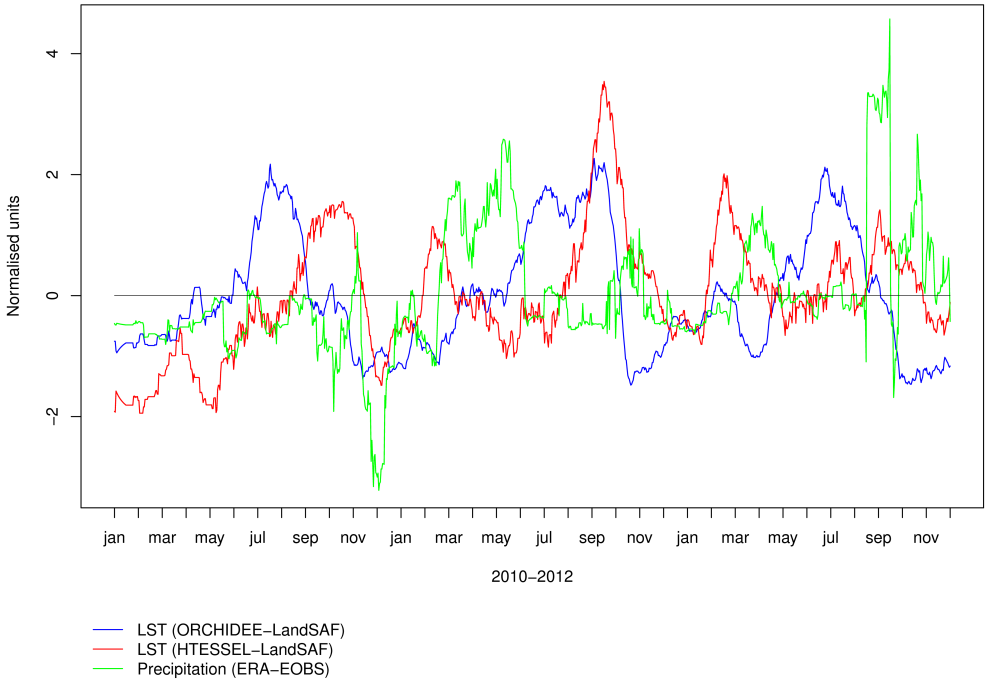

Figure 8. Temporal evolution of the expansion coefficients correspondent to the first EOF variation mode of the LST and the precipitation errors. As in Fig. 5, values have been normalized using the standardization method.

HESSD
12, 13019–13067, 2015

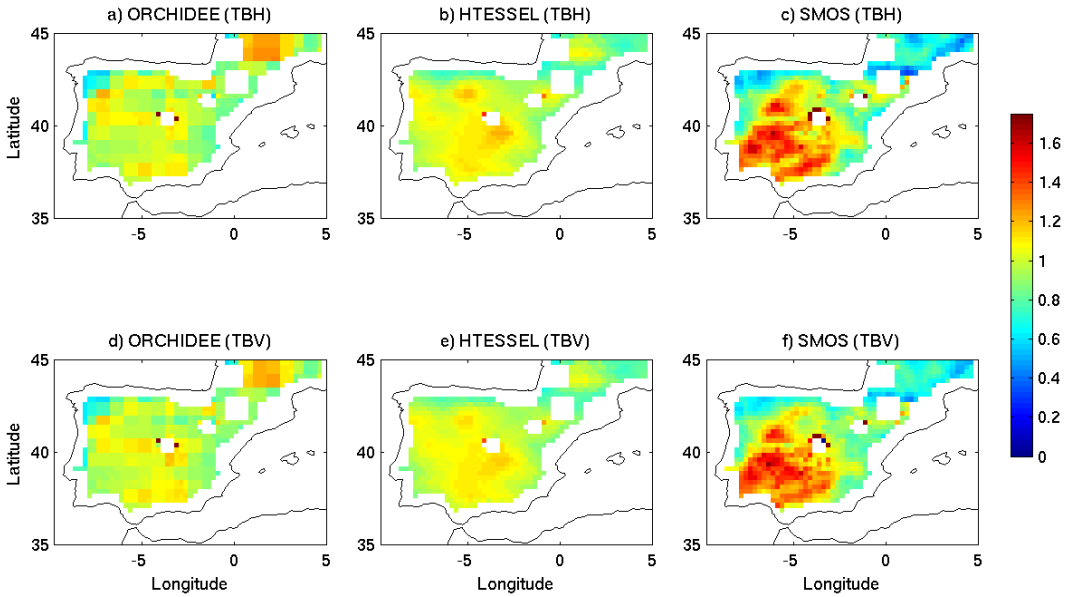

Figure 9. Normalised amplitude of the smoothed annual cycle of modelled and measured TBs: $\frac{\text{amplitude (TB)}}{\overline{\text{TB}}}$. TBH and TBV correspond to the horizontal and vertical polarizations, respectively.

HESSD
12, 13019–13067, 2015

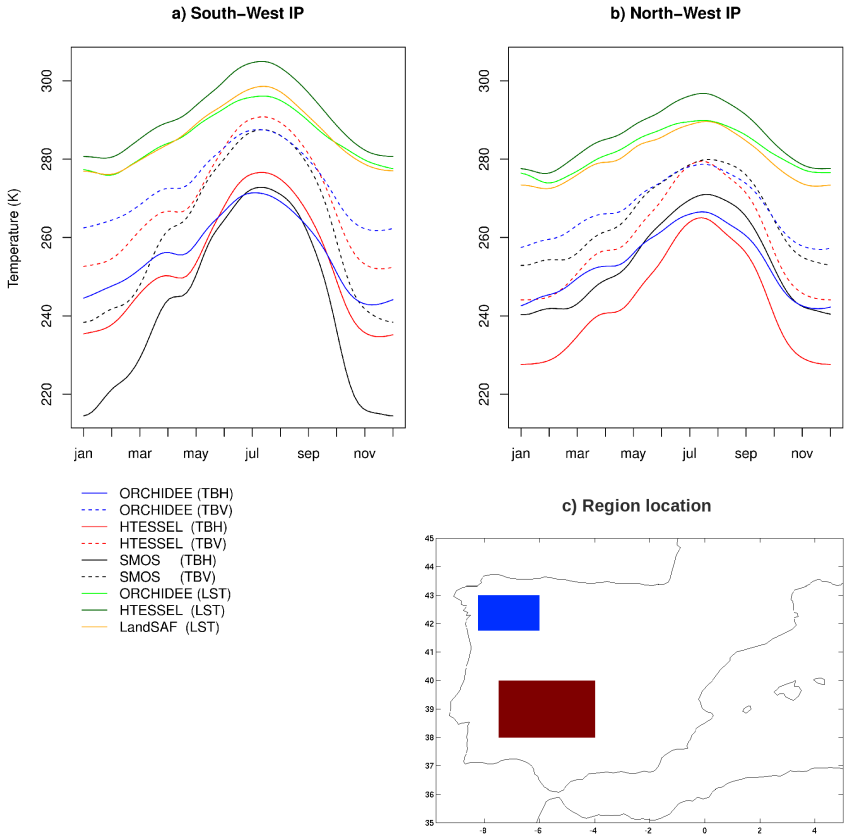

Figure 10. Smoothed annual cycle of TB_{SM}, TB_{OR}, and TB_{HT}, as well as of the LST signals from ORCHIDEE, H-TESSEL, and LandSAF over a South-Western **(a)** and North-Western **(b)** region of the Iberian Peninsula, from 2010 to 2012. The TBH and TBV correspond to the horizontal and vertical polarizations, respectively. The regions' location is shown in **(c)** South-West (red) and North-West (blue).

HESSD
12, 13019–13067, 2015